







Pollutant dispersion by tall buildings: Laboratory experiments and Large-Eddy Simulation

H.D. Lim¹  · Denise Hertwig²  · Tom Grylls³  · Hannah Gough²  · Maarten van Reeuwijk³  · Sue Grimmond²  · Christina Vanderwel^{1*} 

Received: date / Accepted: date

Abstract Pollutant dispersion by a tall-building cluster within a low-rise neighbourhood of Beijing is investigated using both full-scale Large-Eddy Simulation and water flume experiments at 1:2400 model-to-full scale with Particle Image Velocimetry and Planar Laser-Induced Fluorescence. The Large-Eddy Simulation and flume results of this realistic test case agree remarkably well despite differences in the inflow conditions and scale. Tall buildings have strong influence on the local flow and the development of the rooftop shear layer which dominates vertical momentum and scalar fluxes. Additional measurements using tall-buildings-only models at both 1:2400 and 1:4800 scales indicates the rooftop shear layer is insensitive to the scale. The relatively thicker incoming boundary layer affects the Reynolds stresses, the relative size of the pollutant source affects the concentration statistics and the relative laser-sheet thickness affects the spatially averaged results of the measured flow field. Low-rise buildings around the tall building cluster cause minor but non-negligible offsets in the peak magnitude and vertical location, and have a similar influence on the velocity and concentration statistics as the scale choice. These observations are generally applicable to pollutant dispersion of realistic tall building clusters in cities. The consistency between simulations and water tunnel experiments indicates the suitability of both methodologies.

Keywords Large-eddy simulation (LES) · Planar laser-induced fluorescence (PLIF) · Particle image velocimetry (PIV) · Pollutant dispersion · Urban flow · Tall buildings

1 Introduction

Urban landscapes worldwide are extending vertically. The demand for high-rise commercial centres and tall residential buildings is increasing in regions such as Asia due

¹ Aeronautics and Astronautics Department, University of Southampton, UK

² Department of Meteorology, University of Reading, UK

³ Department of Civil and Environmental Engineering, Imperial College London, UK

*Corresponding author. E-mail: c.m.vanderwel@soton.ac.uk

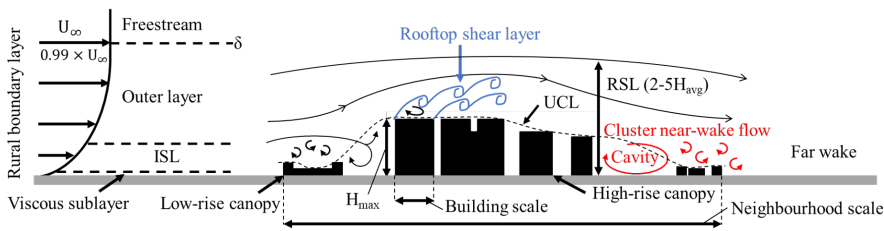


Fig. 1 Dominant flow features of an atmospheric boundary layer flow through an urban neighbourhood. Sketch is not to scale. ISL: Inertial sublayer, RSL: roughness sublayer, H_{avg} : average building height, H_{max} : maximum building height, U_{∞} : freestream velocity, δ : boundary layer thickness.

32 to the scarcity of land and the need to house an increasing urban population close
 33 to their workplaces. Buildings have a profound effect on near-surface atmospheric
 34 processes like airflow and scalar transport (Bitter and Hanna, 2003; Belcher, 2005).
 35 Tall buildings, whether isolated or in clusters, alter and exacerbate such effects.

36 Tall buildings exert their influence on urban processes over a range of spatial scales,
 37 from impacting surroundings buildings (e.g. pressure distributions on façades) and
 38 street canyons (flow-regime changes) to neighbourhoods in the building wake (drag
 39 distribution). The subregions of the atmospheric boundary layer and the dominant flow
 40 features within an urban neighbourhood relevant to both building and neighbourhood
 41 scales are sketched in Fig. 1. At the building scale, the momentum and scalar fluxes
 42 in the roughness sublayer (RSL) are intricately connected to the urban morphology.
 43 Some insights into this can be gained by considering studies of cuboids (i.e., finite-
 44 length square cylinders). For an isolated cube, Oke et al. (2017) describe how the
 45 initial flow field diverges in the vertical and lateral directions to form recirculating
 46 flows on the roof and side walls which reattaches if the building length in the direction
 47 of the flow is greater than its height. The lee of the building is dominated by flow
 48 separation, with the formation of a cavity zone (recirculating flow) and turbulent
 49 wake. Near the ground, horseshoe vortices wrap around the building resulting in high
 50 turbulence intensities that define the lateral boundaries of the wake (Simpson, 2001;
 51 Oke et al., 2017).

52 The height-to-diameter aspect ratio (AR) of isolated obstacles has a strong influ-
 53 ence on the resulting flow field. For an isolated finite-length round cylinder, Tanaka and
 54 Murata (1999) describes how the edge vortices (shed from the sides of the cylinder)
 55 interact with the free-end vortex (shed from the tip), forming the ‘legs’ and ‘heads’ of
 56 the ‘arch’-type vortices in the wake, respectively. While the arch-type vortices match
 57 the outline of the cylinder at $AR = 10$, lower aspect ratio cylinders ($AR \leq 2.5$) have
 58 arch vortices with legs that stretch outwards in the transverse direction and could ex-
 59 tend to several diameters from the cylinder. Base and tip vortices associated with the
 60 bending of the arch-type vortex system are also observed in the near-wake of cuboids
 61 (Wang et al., 2006; Wang and Zhou, 2009). These vortices are closely related to
 62 upwash and downwash effects that can exchange air pollutants between the near-wake
 63 flow and freestream.

64 At the neighbourhood scale, studies of isolated tall buildings within a low-rise
 65 neighbourhood have document the strong impact on the vertical exchange of turbulent

66 and advective momentum and scalars (e.g. [Fuka et al., 2018](#)). Flow and scalar fields
67 in the low-rise canopy are affected by the tall building over large distances ([Brixey
68 et al., 2009](#); [Heist et al., 2009](#)). Likewise, roughness effects of the underlying low-
69 rise canopy can alter the dynamics of the wake zone of tall buildings by breaking
70 down larger vortices ([Hertwig et al., 2019](#)), thus destroying some of the organised
71 motions that have been extensively documented for flow past wall-mounted bluff
72 bodies (e.g. [Castro and Robins, 1977](#); [Hunt et al., 1978](#)). Figure 1 illustrates this scale
73 interaction in the context of an oncoming rural turbulent boundary layer impacting a
74 tall-building cluster within a low-rise neighbourhood. In this, the upstream low-rise
75 canopy influences the incoming flow that impacts the tall building to create the rooftop
76 shear layer, and the tall buildings' wake interacts with the downstream low-rise canopy
77 to alter the cluster near-wake dynamics.

78 Such scale interactions represent a challenge for urban land surface modelling.
79 City-wide neighbourhood scale approaches to modelling the urban canopy layer
80 (UCL) and urban air pollution do not resolve the buildings explicitly, but instead
81 rely on concepts applicable to simple canonical flows like rough-wall boundary lay-
82 ers or two-dimensional street-canyons of uniform height ([Masson, 2006](#); [Grimmond
83 et al., 2009](#)), in which dynamics in the UCL and RSL are decoupled from processes in
84 the inertial sublayer (ISL), which is assumed to be well-developed. Next-generation
85 regional numerical weather prediction models will have resolutions of $\mathcal{O}(100\text{ m})$ or
86 higher and hence operate within the building grey-zone ([Barlow et al., 2017](#); [Lean
87 et al., 2019](#)), in which the grid resolution approaches the building length scale(s).
88 Sub-grid scale variability becomes large and bulk urban morphology characteristics
89 can differ vastly between grid-boxes ([Kanda et al., 2013](#); [Kent et al., 2019](#)).

90 Large variations in building heights (e.g. tall buildings within a low-rise neigh-
91 bourhood) extend the vertical structure of the UCL but also make its depth less
92 well defined. Aerodynamic roughness length and displacement height used in clas-
93 sic similarity frameworks are typically derived from methods assuming idealised
94 uniform-height building arrays (e.g. [Macdonald et al., 1998](#)). The [Kanda et al. \(2013\)](#)
95 modification recognises the impact of tall buildings and building-height variability on
96 the displacement height in realistic urban settings, resulting in displacement heights
97 that are much larger than derived with conventional methods ([Kent et al., 2017](#)). [Sützl
98 et al. \(2021\)](#) show that dispersive fluxes in the RSL become important in spatially-
99 averaged budgets when strong vertical and horizontal heterogeneity in an urban area
100 exists, supporting the argument that dispersive stresses should be represented to im-
101 prove urban canopy models (e.g. [Giometto et al., 2016](#)).

102 Such model development needs can only be addressed by having suitable data to
103 derive and test parametrisations. Turbulence-resolving Computational Fluid Dynam-
104 ics (CFD) methods, like Large-Eddy Simulation (LES), can provide valuable insight
105 into the spatio-temporal structure of urban flow fields (e.g. [Letzel et al., 2008](#); [Tolias
106 et al., 2018](#)), but model output needs to be evaluated carefully through comparison
107 with suitable observations. Complementary to CFD approaches, laboratory experi-
108 ments using scale models in low-speed wind tunnels or water flumes are valuable for
109 urban flow and dispersion studies, as they offer flexibility in model design and full
110 control of inflow and boundary conditions. The reduction in physical complexity (*cf.*
111 field observations) make laboratories ideal for systematic studies of urban processes

(e.g. Baik et al., 2000; Pournazeri et al., 2012; Di Bernardino et al., 2015). However, laboratory studies involve uncertainties inherent to the facility type, measurement technique or choice of model scale (e.g. Wang et al., 1996; Saathof et al., 1995; Kanda, 2006), which have to be quantified and considered carefully when analysing and interpreting the results (Torres et al., 2021).

This study explores the important features of the flow and dispersion around a cluster of tall buildings surrounded by a low-rise canopy, using a Beijing neighbourhood as a case study (Sect. 2.1). Uniform arrays of buildings have been studied in the past, but the results are not always applicable to realistic urban geometries (Vanderwel and Ganapathisubramani, 2019), hence motivating this study as cities become increasingly critical to simulate for a wide range integrated urban services (Grimmond et al., 2020). The few studies that have considered realistic urban settings with tall building clusters have mainly focused on wind loads (Nozu et al., 2015; Yan and Li, 2016; Elshaer et al., 2017). Here we use both water-flume experiments (Sect. 2.2) and LES (Sect. 2.3) to demonstrate their capabilities in a realistic scenario and to explore the effect of the tall-building cluster on the flow structure and scalar transport (Sect. 3).

We use this case study to explore fundamental questions relating to the methodologies and physical processes of realistic urban geometry flow. Although thermal stratification and differential heating have been demonstrated to influence flow and dispersion in idealised urban environments studies (Nazarian et al., 2018; Marucci and Carpentieri, 2020), in this more realistic geometry study we only consider neutral atmospheric stability (i.e., Richardson number is close to zero), and therefore negligible buoyancy effects. In Sect. 3.1, we focus on the scale dependency of the flume results. In Sect. 3.2, we explore the physical flow structure and scalar distribution in the cluster wake and discuss the suitability and limitations of flume experiments and LES. In Sect. 3.3, we investigate the impact of low-rise neighbourhood buildings on the cluster wake in the flume. In our conclusions section (Sect. 4), we discuss that our findings provide important and applicable results for real cities that are of concern for weather extremes and climate change; as well as make recommendations for future scaled experiments and LES methodologies.

2 Methodology

2.1 Study area

The Haidian District is a typical residential–commercial area in Beijing, with a cluster of 14 tall buildings surrounded by a low-rise neighbourhood. To characterise this area in the laboratory experiments, we used three scale models (Fig. 2a-c) with a test area of ~580 m full-scale extent (for details see Hertwig et al., 2021). This neighbourhood was represented by 3D-printed models (Hertwig et al., 2020) which contain all main building structures with small geometrical simplifications at two geometric scales (1:2400 and 1:4800):

1. **LT2400** (1:2400 model scale; Fig. 2a) is a detailed model of low-rise buildings and the tall-building cluster. The low-rise buildings are binned at three heights based on a modal analysis of the neighbourhood: $H_{min,LT2400} = 2$ mm (4.8 m at

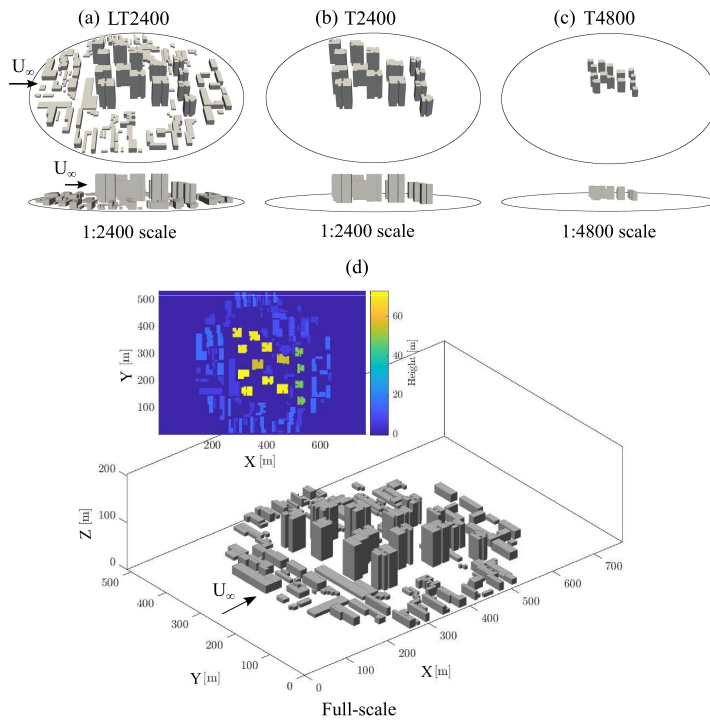


Fig. 2 3D-printed reduced-scale urban models used in the water-flume (circle indicates model ground plate extent): (a) LT2400, (b) T2400 and (c) T4800; and (d) LES at full-scale with computational domain for LT2400. For each case the inflow (U_∞) is from the North (arrows).

- 154 full-scale), 4 mm (9.6 m), and 6 mm (14.4 m). The height of the tall elements is
 155 between 20 mm (48 m) to $H_{max,LT2400} = 30$ mm (72 m).
- 156 2. **T2400** (1:2400; Fig. 2b) only has the tall building cluster without the low-rise
 157 surroundings. The height of the tall elements is between $H_{min,T2400} = 20$ mm
 158 (48 m) to $H_{max,T2400} = 30$ mm (72 m).
- 159 3. **T4800** (1:4800; Fig. 2c) uses the same geometry as T2400, but at a reduced scale
 160 so that the heights of the tall elements range between $H_{min,T4800} = 10$ mm (48 m)
 161 and $H_{max,T4800} = 15$ mm (72 m).

162 In the LES, the modelled buildings are the same as the LT2400 model (Fig. 2d) but
 163 simulations are performed at full-scale. For both the flume and the LES data, results
 164 are presented using a Cartesian coordinate system in which X is the streamwise, Y
 165 the lateral and Z the vertical direction (Fig. 2d, 3), with corresponding instantaneous
 166 velocities u , v and w . Time-averaged variables are given in uppercase such that, e.g.,
 167 $u = U + u'$, where the prime indicates the fluctuation about the mean.

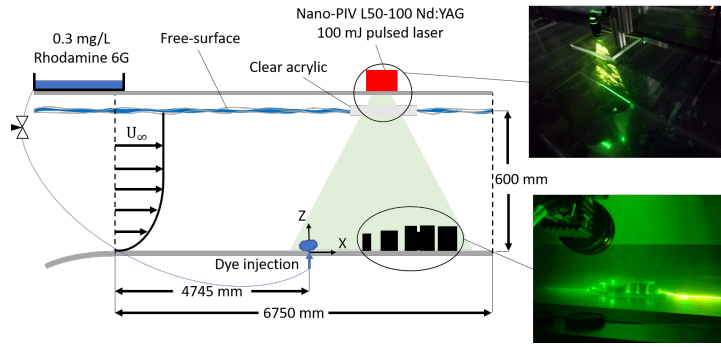


Fig. 3 Particle Image Velocimetry (PIV) and Planar Laser Induced Fluorescence (PLIF) setup in the water flume. Images (right) show the laser sheet directed through an acrylic sheet mounted at the water surface onto the 3D-printed urban model.

168 2.2 Water tunnel experimental methodology

169 The University of Southampton's water flume facility has a test section that is
 170 6,750 mm long and 1,200 mm wide (Fig. 3). Throughout the measurement campaign,
 171 the water depth and free-stream velocity are maintained at a constant level of
 172 600 ± 1 mm and $U_{\infty\text{EXP}} = 0.46$ m s⁻¹. The 3D urban model is fixed to a smooth
 173 acrylic 'false floor' that overlies the entire length of the test section glass bottom.
 174 Building configurations analysed in this study are aligned to have an inflow direction
 175 from North.

176 Vertical profiles of the incoming flow (Fig. 4) fit a power law description of the
 177 boundary layer, $U/U_{\infty\text{EXP}} = (Z/\delta_{\text{EXP}})^{\alpha}$, with an exponent of $\alpha \approx 0.11$, which is
 178 typical of rural or rural-to-urban terrain flows (Tomas et al., 2017). The incoming
 179 flow boundary layer thickness is $\delta_{\text{EXP}}=83$ mm based on the definition of $0.99U_{\infty}$.
 180 The friction velocity is $U_{\tau\text{EXP}}=0.0173$ m s⁻¹ $\pm 10\%$ (Appendix A). The logarithmic
 181 region is found to be valid from approximately $0.04 < Z/\delta_{\text{EXP}} < 0.22$, consistent
 182 with smooth wall turbulent boundary layers.

183 To reproduce the turbulence scales of full-scale sharp-edged buildings (fixed
 184 separation points) and achieve Reynolds number independence, the Reynolds number
 185 (based on building height) should be greater than 5,000–10,000 (Plate, 1999). Here,
 186 based on the tallest building height and $U_{\infty\text{EXP}}$, $Re \approx 14,000$ for the 1:2400 scale
 187 model and $Re \approx 7,000$ for the 1:4800 scale model. These should be sufficiently large
 188 to reproduce the turbulent characteristics of the full-scale flow.

189 Two-dimensional Particle Image Velocimetry (PIV) and Planar Laser Induced
 190 Fluorescence (PLIF) measurements are performed simultaneously to obtain velocity
 191 and concentration measurements in the streamwise plane. The spanwise position (Y
 192 location) of the measurement plane is at the flume's centre-plane (i.e., at maximum
 193 distance from the flume's side walls) to avoid any potential flow asymmetry due to
 194 the boundary layers of the side walls. For the wind direction analysed here, the plane
 195 is located in the middle of one of the tallest building to investigate its influence on
 196 the wake flow (Fig. 2). For the PIV measurements (Appendix B), the flow is seeded

197 with 50 μm polyamide seeding particles, and allowed to recirculate in the flume until
198 the desired seeding density and uniform particle distribution is achieved. Illumination
199 is provided by a 100 mJ Nd:YAG double-pulsed laser with an emission wavelength
200 of 532 nm operated at 4 Hz. Two 4 MP CMOS cameras are used in a side-by-side
201 configuration to achieve a field-of-view of 230 mm streamwise \times 135 mm vertical.
202 LaVision's Davis 8.4.0 software (LaVision GmbH, 2019) is used to acquire and
203 process the images.

204 For the PLIF measurements, a neutrally buoyant solution of Rhodamine 6G fluo-
205 rescent dye with concentration levels of $C_S=0.3 \text{ mg L}^{-1}$ is continuously introduced to
206 the flume at ground level, 5 mm upstream of the model plate using a 3 mm diameter
207 tube. The dye flow rate is maintained at a constant rate ($30 \text{ cm}^3 \text{ min}^{-1}$) by a needle
208 valve to ensure minimal disturbance to the flow in the flume. The dye Schmidt number
209 ($Sc=2500\pm300$, (Vanderwel and Tavoularis, 2014)) indicates momentum diffuses at
210 a much higher rate than the scalar. The absorption and emission peaks of Rhodamine
211 6G are 525 nm and 554 nm, respectively. An optical long-pass filter with a sharp cutoff
212 (540 nm) is used to block out incident light from the laser and reflected light from
213 the PIV particles. This filter is in front of the 5.4 MP 16-bit depth sCMOS camera
214 used to record the fluorescence emitted from the excited dye. Local concentrations are
215 determined from the fluorescence intensity in a calibration procedure (Appendix C).

216 2.3 LES methodology

217 The uDALES model (Tomas et al., 2015; Grylls et al., 2019) is a high-resolution, large-
218 eddy simulation (LES) code for simulation of the urban environment atmospheric
219 boundary layer. LES models resolve the flow at the energetically dominant scales of
220 turbulent motion by filtering the Navier-Stokes equations. They are therefore able to
221 resolve the unsteady nature of turbulent flows unlike Reynolds-averaged Navier-Stokes
222 models while being less computationally intensive than direct numerical simulation
223 techniques. LES provides an optimal tool to model the spatial and temporal scales
224 necessary to investigate both the urban micro-scale environment and the atmospheric
225 boundary layer.

226 uDALES is adapted from the Dutch Atmospheric Large-Eddy Simulation model
227 (DALES) (Heus et al., 2010). Buildings are modelled using the immersed boundary
228 method (Tomas et al., 2015). Log-law wall functions are implemented to capture the
229 near-wall dynamics (Uno et al., 1988; Suter, 2018). The gradient diffusion hypothesis
230 is used to close the subgrid scale terms following the approach of Vreman (2004) and
231 Suter (2018). uDALES uses finite differences with variables spatially discretised on an
232 Arakawa C-grid. A second-order differential scheme is applied to all field variables
233 except the pollutant fields. The latter uses a kappa scheme to ensure positivity. A
234 third-order Runge-Kutta time integration scheme is applied (Heus et al., 2010; Grylls,
235 2020).

236 The flow conditions of the flume experiments just upstream of the building cluster
237 are reproduced in an approximate manner by using a driver simulation with a domain
238 size of $768\times512\times203 \text{ m}$ (Table 1). The vertical height of the domain matches the
239 estimated boundary layer depth of the 1:2400 scale water tunnel experiment ($\delta_{\text{EXP}} \approx$

Table 1 LES parameters for the driver and verification simulations, where P indicates periodic boundary conditions (BC) and I inflow-outflow BC.

Simulation	Grid size	Domain size	$U_{\tau LES}$	Run-up	Averaging period	X BCs	Y BCs
	[-]	[m]	[$m s^{-1}$]	[s]	[s]		
Driver	576×384×192	768×512×203	0.106	122400	28800	P	P
Verification	576×384×192	768×512×203	0.106	3600	25200	I	P

83 mm) at full scale ($\delta_{LES} = 203$ m). Periodic boundary conditions are employed for the lateral boundaries. A free-slip condition is applied at the top of the domain and wall functions are applied at the façades of the immersed boundaries. Neutral atmospheric conditions are enforced. The simulation is forced by a constant pressure gradient. A spin-up period of 122,400 s is used to allow the flow field to reach a statistical equilibrium, after which data are analysed for 28,800 s. During this period, the velocity fields at the outlet plane ($X = 768$ m) are saved every second for use as the inlet boundary condition for the verification simulation (Table 1).

The driver simulation is designed to produce a rural boundary layer with a roughness length $Z_0 = 0.5$ m. Since this roughness length is of similar order of magnitude to the cell size in the LES, the use of a smooth wall with a wall function is not suitable. Therefore, the Macdonald et al. (1998) relation is used to estimate the parameters that reproduce Z_0 using an array of staggered cubes. With a packing density of 0.125 and block height of 3.2 m a roughness length of 0.5 m is obtained. The flow friction velocity is increased in the full-scale LES application to $U_{\tau LES} = 0.1055$ $m s^{-1}$. The roughness length applied to the individual blocks is 0.05 m. The freestream velocity is $U_{\infty LES} = 1.94$ $m s^{-1}$.

The velocity and Reynolds shear stress profiles show reasonably good agreement between the experiments and LES results (Fig. 4). The quasi-linear Reynolds shear stress profile of the LES data is expected by definition when the flow is in statistical equilibrium. The velocity profiles match well, except near the wall where the difference between flume and LES (smooth vs rough-wall turbulent boundary layer) becomes evident.

The outflow plane from the driver simulation is used as input at the inlet of the verification simulation. The verification simulation uses inflow-outflow boundary conditions in the X -direction. Therefore, this resembles the water flume with the boundary layer flow upstream developing in the streamwise direction as it is transported over the model rig. The first 3,600 s are spin up, the data analysed are the next 25,200 s. To simulate the pollutant release upwind of the urban area, a continuous point source is introduced at the origin $X=0$ with strength $\dot{M} = 1$ $g s^{-1}$. The source is introduced directly in the advection-diffusion equation and does not affect the velocity field (no injection of fluid). To compare the flume and LES results, the concentrations are scaled by the source concentration C_s . Without C_s in the LES, this is obtained by matching the mean concentration profiles at $X/\delta=0.5$. This scaling is permitted as the advection-diffusion equation is linear with concentration C .

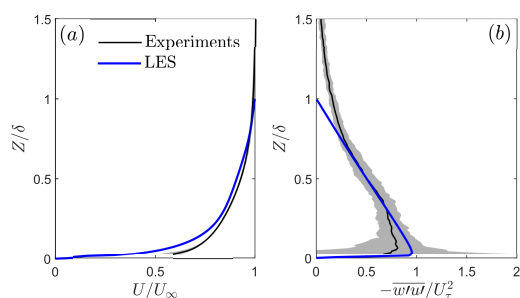


Fig. 4 Water flume and LES incoming flow vertical profiles (time- and spatial-mean) of: (a) streamwise velocity and (b) Reynolds shear stress with 5th and 95th percentile (shading) bounds of experimental data. Flume and LES data are normalized by their respective $U_{\infty\text{EXP}}$, $U_{\tau\text{EXP}}$, δ_{EXP} , $U_{\infty\text{LES}}$, $U_{\tau\text{LES}}$ and δ_{LES} .

3 Results and discussions

3.1 Scale-dependency of flume results

The simplified tall-building cluster (without low-rise buildings) at two scales (T2400, T4800) is used to gain insight into the influence of geometrical scale on the velocity and scalar fields measured. The mean velocity, velocity variance, Reynolds shear stress, mean concentration, concentration variance, turbulent scalar flux and advective scalar flux maps are shown in Fig. 5 for both scales of model. To account for the scale difference, the streamwise and vertical axes are non-dimensionalized by the height of the tallest buildings in each model.

In the mean velocity and velocity variance contours for the T2400 (Fig. 5a,b(i)), the growth and development of a rooftop shear layer originating from the tall building at approximately $X/H_{\text{max},T2400} \simeq 4$ is evident, as is the recirculating flow region in the urban canopy layer and on the leeward side of the cluster ($X/H_{\text{max},T2400} > 6$). The same observations can be made for T4800 (Fig. 5a,b(ii)) but the recirculating flow region does not extend beyond $X/H_{\text{max},T4800} > 8$. The Reynolds shear stress contours (Fig. 5c) and vertical profiles (Fig. 6c) have good agreement with the peaks in the vertical profile corresponding to the rooftop shear layer, but T2400 has greater peak magnitudes than T4800.

The mean concentration and concentration variance results have similar characteristics for both T2400 and T4800, but the vertical profiles (Fig. 6d,e) show qualitative and quantitative differences with higher magnitudes at all streamwise location for T4800. Near the source, where the dye concentration is still very high, the dye response is no longer linear and secondary fluorescence creates a ‘halo’ effect that is noticeable in the flume measurements (Fig. 5d,e(i,ii)). Based on Vanderwel and Tavoularis (2014) and Baj et al. (2016), this local concentration bias is estimated to be up to 60%. However, this is expected to be negligible further from the source hence no correction is applied. The larger variability in the concentration contours also reflects the inherent uncertainty of the scalar transport that is dominated by a few large events (Fig. 5e). The corresponding profiles (Fig. 6e) are somewhat ‘fuzzy’, as is typical in

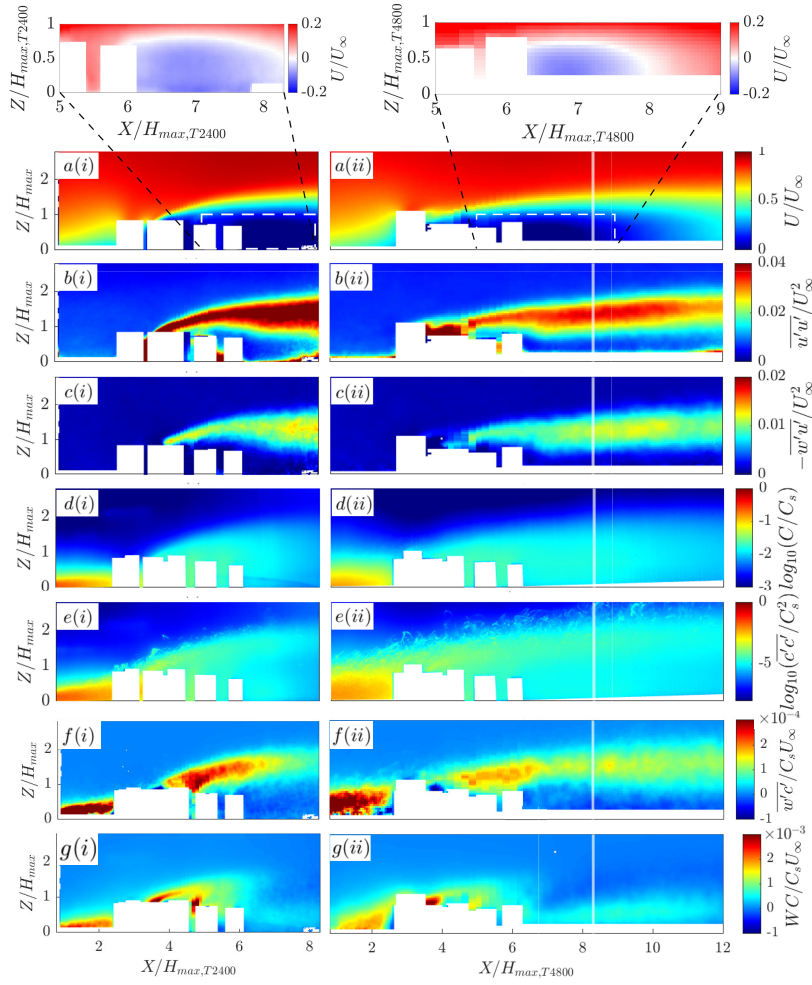


Fig. 5 Water-flume contours for the (i) T2400 and (ii) T4800 cases (Fig. 2b,c) normalized by their respective length scales (Section 2.1), showing (a) mean velocity, (b) velocity variance, (c) Reynolds shear stress, (d) mean concentration, (e) concentration variance, (f) turbulent scalar flux and (g) advective scalar flux. Insets (a) show the recirculating flow in the cluster near-wake region. T4800's vertical white lines indicate the outflow boundary for the T2400 case.

304 highly intermittent scalar fields measured for limited duration with thin dye plumes.
 305 It is attributed to non-Gaussian, highly skewed probability density functions of the
 306 scalar fluctuations (Vanderwel and Tavoularis, 2016).

307 The turbulent scalar flux (Fig. 5f, 6f) appears to be concentrated along the rooftop
 308 shear layer, suggesting the presence of instabilities that contribute significantly towards
 309 the vertical exchange of scalars. Near the building cluster, the advective scalar flux
 310 magnitudes (Fig. 5g, 6g) are higher than the corresponding turbulent scalar flux
 311 components (Fig. 5f, 6f) due to strong updrafts and downdrafts. Downwind of the
 312 building cluster, the magnitudes of the advective scalar flux decreases quickly and

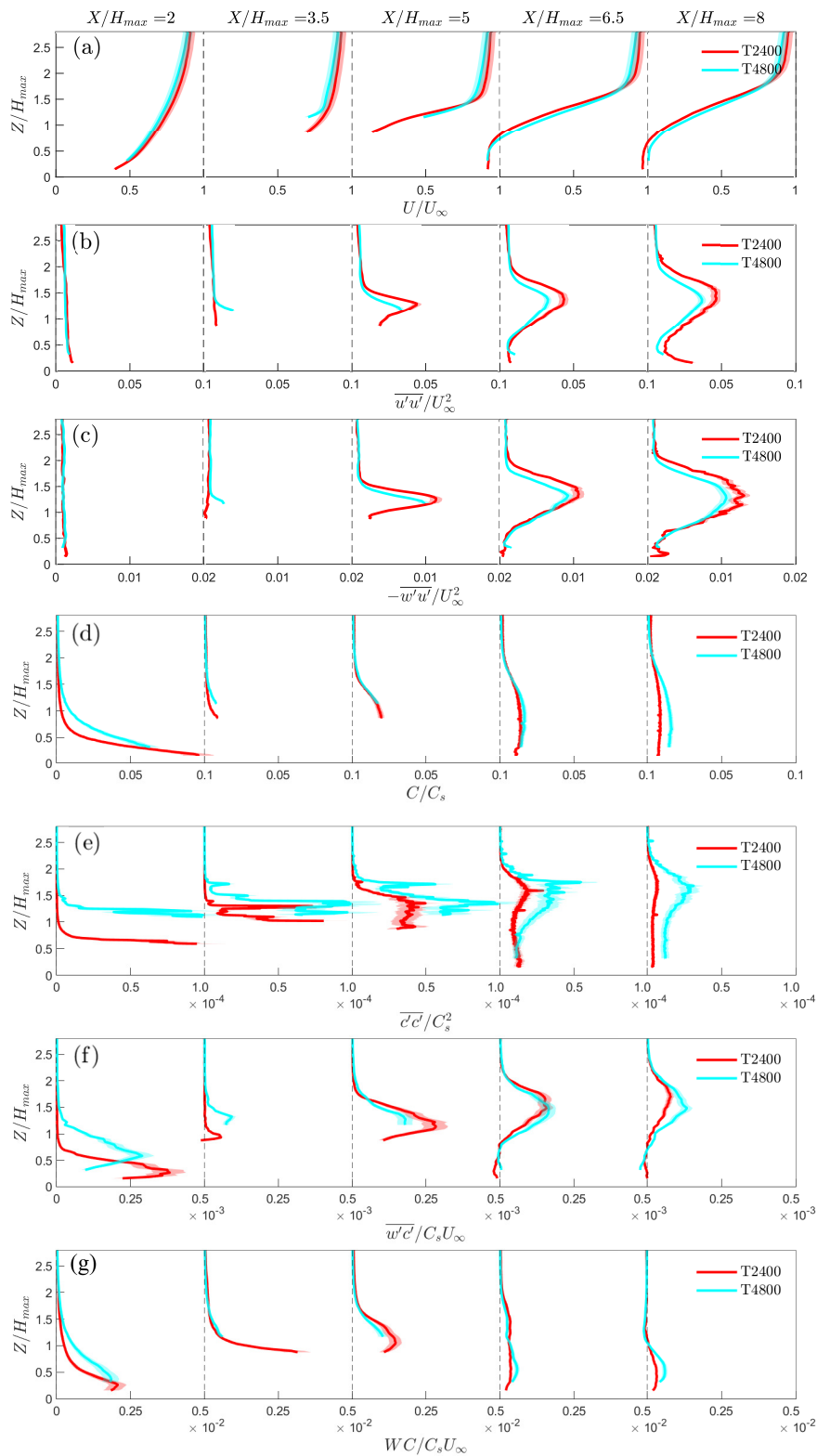


Fig. 6 Water-flume vertical profiles for T2400 and T4800 normalized by their respective length scales (Section 2.1), showing (a) mean velocity, (b) velocity variance, (c) Reynolds shear stress, (d) mean concentration, (e) concentration variance, (f) turbulent scalar flux and (g) advective scalar flux extracted at regular streamwise intervals. Uncertainties (shading) are based on the sum of random and bias errors at 95% confidence interval (Appendices B, C).

313 do not appear to be associated with the rooftop shear layer which persists for much
 314 further downstream distances. The contribution of the turbulent scalar flux to the total
 315 scalar transport increases in this shear-dominated region.

316 3.1.1 Implications of model scale for flume experiments

317 The size of the flume facility and domain size of interest influences the choice of
 318 geometrical scales for hardware models. However, the scale choice has several con-
 319 sequences on the velocity and scalar fields measured that need to be considered when
 320 interpreting the results.

321 In this experimental campaign, the dye source size and position relative to the
 322 model centre are fixed. Changing the model scale changes the effective size and
 323 location of the dye plume source relative to the building height. This leads to a larger
 324 incoming plume width relative to the building height for T4800 *cf.* T2400, which
 325 is evident in the concentration statistics (Fig. 5d,e) and the corresponding vertical
 326 profiles at $X/H_{max}=2$ (Fig. 6d,e), where the T4800 profiles have a vertical offset *cf.*
 327 T2400. This likely contributes to the discrepancies in the scalar statistics, where the
 328 means and variances are larger for T4800 *cf.* T2400.

329 Based on the concentration statistics (Fig. 6), the concentration variance is the
 330 most sensitive variable to the effects of scale. There are implications for air quality
 331 modelling where peak-to-mean concentration levels are of interest. When we non-
 332 dimensionalize the concentration variance using the building height and source prop-
 333 erties following Sessa et al. (2018), the vertical profiles of the cluster near-wake flow
 334 do not collapse. While meandering is the main source of concentration fluctuations in
 335 Fackrell and Robins (1982b) much simpler application involving an elevated source in
 336 smooth-wall turbulent boundary layers, the complex/realistic urban landscape in this
 337 study introduce non-linear effects on the concentration fluctuations. The source size,
 338 relative to the turbulence lateral integral scale, has a large effect on the concentration
 339 fluctuations (Fackrell and Robins, 1982a), but it is unclear what effect the interaction
 340 of a ground source with a complex urban landscape has on the concentration fluctua-
 341 tions. We are unaware of any empirical expression in the literature that will normalize
 342 the concentration statistics in complex urban flows. Accounting for the model scale
 343 for concentration fluctuations requires consideration of the lateral turbulence scales
 344 near the ground and investigating the non-linear interaction of these scales with the
 345 urban landscape. These are non-trivial problems that are currently being investigated.

346 The change in model scale makes the laser sheet proportionally thicker (in the
 347 lateral Y direction) for T4800 than T2400, hence covering a wider non-dimensional
 348 Y -section within the urban model, thus expanding the spatial averaging effect within
 349 the derived statistics. In very heterogeneous urban settings (as this study), flow and
 350 scalar fields have a large spatial variability so the laser sheet thickness impacts the
 351 processes sampled. For example, the tall building at $X/H_{max,T2400} \simeq 3$ does not affect
 352 the measured flow field for T2400 because it is in front of the laser sheet (Fig. 5a,b(i)),
 353 while the same building at $X/H_{max,T4800} \simeq 3$ has an effect on flow within the laser
 354 sheet for T4800 resulting in strong effects on the flow statistics in the measurement
 355 plane (Fig. 5a,b(ii)). This highlights that in geometrically complex settings and at
 356 small model scales, a relatively thick laser sheet can have a significant impact on

357 what the measurements represent. There is a practical limit to the minimal width of
358 the laser sheet (typically around 1 mm) after taking into account in- and out-of-plane
359 movements of the seeding particles. Hence, using a very small scale model that is
360 expected to generate highly three-dimensional flow features can lead to significant
361 spatial averaging effects which needs to be considered when interpreting the results.

362 3.1.2 Influence of the incoming boundary layer conditions

363 As both the mean velocity and turbulence properties of the incoming flow impinging
364 on the T2400 and T4800 models effectively differ, comparing the flow fields of these
365 two cases is expected to reveal the effect of immersing the tall buildings in different
366 parts of the approach boundary layer flow. With a change in fetch from rural-to-urban,
367 the first buildings will typically extend into the logarithmic region of the oncoming
368 rural atmospheric boundary layer. In the flume, the depth of the logarithmic region
369 of the incoming flow extends to ~ 18 mm (Appendix B), which translates to ~ 43 m
370 (T2400, LT2400) and ~ 86 m (T4800), respectively, in full scale. This has the following
371 implications for the cases investigated:

- 372 – **T2400**: All tall buildings extend beyond the logarithmic region of the inflow
373 boundary layer.
- 374 – **T4800**: All tall buildings are within the logarithmic region.

375 The mean velocity, velocity variance and Reynolds stress (Fig. 6a-c) match well
376 at all streamwise locations with only minor differences in the magnitudes which
377 show that the velocity shear created at the rooftop of the tall building dominates
378 over differences in the background turbulence in the outer and logarithmic layer. This
379 hypothesis is further supported by the well-matched turbulent scalar flux profiles
380 (Fig. 6f). Near the source (at $X/H_{max} = 2$), there is a mismatch in the height of the
381 peak due to the difference in the relative source size (Section 3.1.1). These profiles
382 align after the oncoming flow encounters the first tall building in the measurement
383 plane ($X/H_{max} \geq 5$), which illustrates the dominating influence of the tall building.

384 Insights into the slightly larger magnitudes of velocity variance and Reynolds
385 stress for T2400 *cf.* T4800 can be gained by comparing the results of our study to
386 cuboid flows literature. Wang et al. (2006) show that as the boundary layer thickness
387 increases, the base vortices are enhanced, leading to stronger upwash flow that weakens
388 the downwash effects of the free-end shear layers. This leads to a decrease in the
389 Reynolds stresses near the ‘ground’ and an increase near the free-end of the cuboid
390 (i.e., ‘roof’). Given the T4800 buildings are shorter (*cf.* T2400, w.r.t. δ_{EXP}), the
391 incoming boundary layer is proportionately deeper. This could explain the lower
392 Reynolds stresses observed throughout the entire building height in the near-wake
393 flow region of T4800 ($Z/H_{max} < 1$ in Fig. 6b,c). The lack of high Reynolds stresses
394 near the rooftop may be attributed to several differences between Wang et al. (2006)
395 and our study: (1) the buildings in the Beijing models are geometrically much more
396 complex and form a cluster, (2) the cuboid height-to-diameter aspect ratio ($AR = 5$) in
397 Wang et al. (2006) is slightly larger than in this case ($AR < 3$), and (3) the boundary
398 layer thickness is less than the cuboid’s height in Wang et al. (2006).

399 The vortex lines of individual buildings are expected to be similar to those observed
400 by [Tanaka and Murata \(1999\)](#) with a wide lateral spread of the legs that extend several
401 diameters from a round cylinder of comparable AR. Coupled with the arrangement
402 of the buildings in close proximity to each other, this is expected to result in the
403 vortex lines of different buildings interacting with each other thus creating a much
404 more complex flow scenario than a single cuboid ([Wang et al., 2006](#)). [Nicolai et al.](#)
405 ([2020](#)) demonstrate that flow around a cluster of round cylinders has similar features
406 to a single cylinder, with free-end shear layer created along the roof-line and mixing
407 layers formed at the sides of the cluster. The cluster porosity breaks up the coherence
408 and the wake flow is subject to greater turbulence. As city flow combines the effects
409 of individual buildings, the change in the oncoming boundary layer thickness is
410 expected to influence the interactions of all these vortex lines, resulting in the observed
411 differences in the near-wake flow between T2400 and T4800.

412 3.2 Flume experiment and LES

413 Flume and LES data for the LT2400 (Fig. 2a,d) case are analysed to cross-verify the
414 different methodologies. Comparisons of flow and dispersion variables are presented
415 as both maps (Fig. 7) and vertical profiles (Fig. 8) with the dye source location defined
416 as the origin in both. Note, LES data are available for the complete plane, but the
417 flume data have a reduced field-of-view when buildings in front of the laser sheet
418 block the view into some street canyons.

419 The flow fields for the flume and LES are remarkably similar even though the
420 flume experiments and LES are performed at different scales with slightly different
421 incoming flow conditions (Fig. 4). The mean velocity contours (Fig. 7a) both indicate
422 the development of a strong velocity shear zone from the rooftop of the tall building
423 (rooftop shear layer) farthest upstream ($X/\delta \simeq 1.25$). The velocity variance and
424 Reynolds shear stress contours (Fig. 7b,c) also show two clear boundaries originating
425 from the roof of the first tall building, consistent with the location of the strong velocity
426 shear generated from the rooftop. The flume and LES agree well with each other in
427 both location and magnitude. The separated shear layers from the roof defines the
428 boundaries of the rooftop shear layer (Section 3.2.1).

429 At $X/\delta=1$, a tall building located in front of the laser sheet is masked out in the
430 flume results (Fig. 7a(i)). For the corresponding LES results (Fig. 7a(ii)) masking is
431 unneeded, allowing locally accelerated flow redirected to the side of the building to
432 be observed. At $X/\delta=2$, the region near the ground has slightly larger differences for
433 the vertical profiles of the velocity statistics (Fig. 8a-c). This is attributed to larger
434 localised experimental uncertainty as the region is surrounded by two tall buildings and
435 near-ground measurements are notoriously difficult to acquire with high confidence
436 with the PIV technique. Challenges include shadows, laser reflections and buildings in
437 the foreground blocking the camera's line-of-sight, which can lead to missing velocity
438 information in this region. In the near-wake of the tall-building cluster at $X/\delta \approx 2.5$,
439 backward flow is observed to extend from the ground to roof level of the tall building
440 (72 m; Fig. 8a and Fig. 7a insets). Reattachment is not observed in the flume or LES
441 domain.

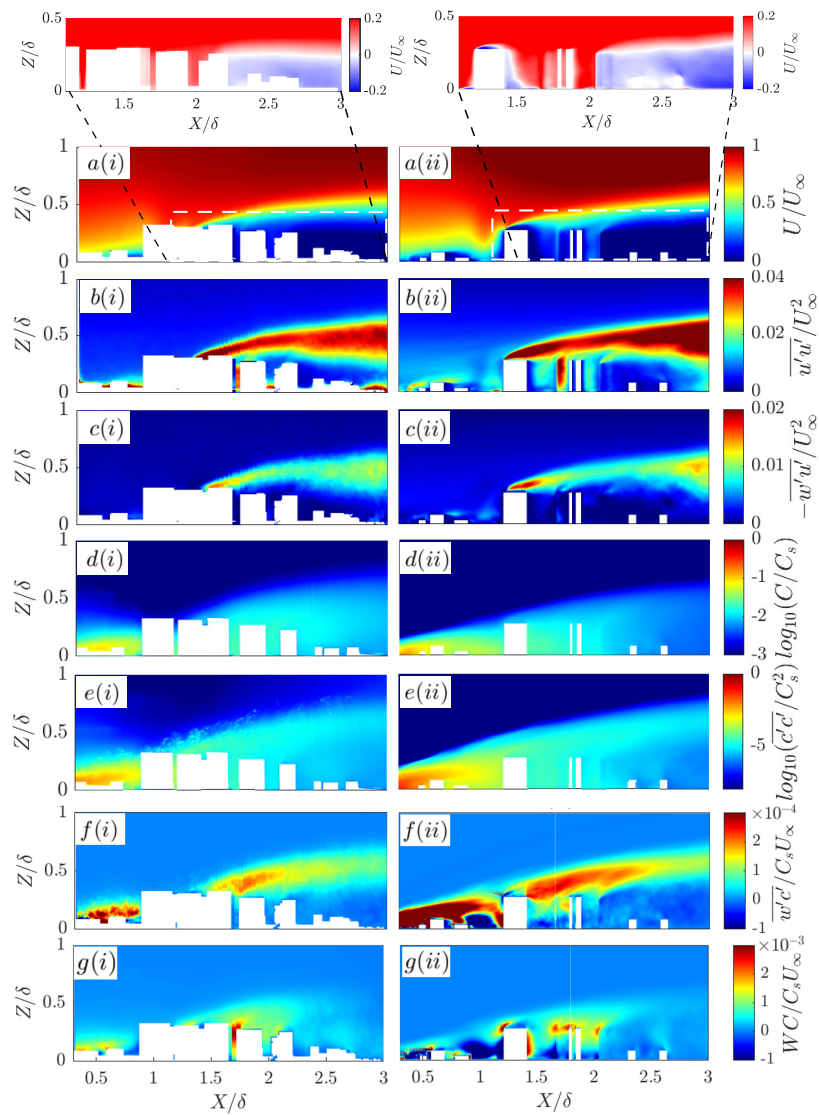


Fig. 7 Contours for the LT2400 case (Fig. 2a,d) showing (a) mean velocity, (b) velocity variance, (c) Reynolds shear stress, (d) mean concentration, (e) concentration variance, (f) turbulent scalar flux and (g) advective scalar flux for (i) flume and (ii) LES data normalized by their respective length and velocity scales (Section 2.2, 2.3). Insets (a) show the recirculating flow on the roof of the tall building and in the cluster near-wake region.

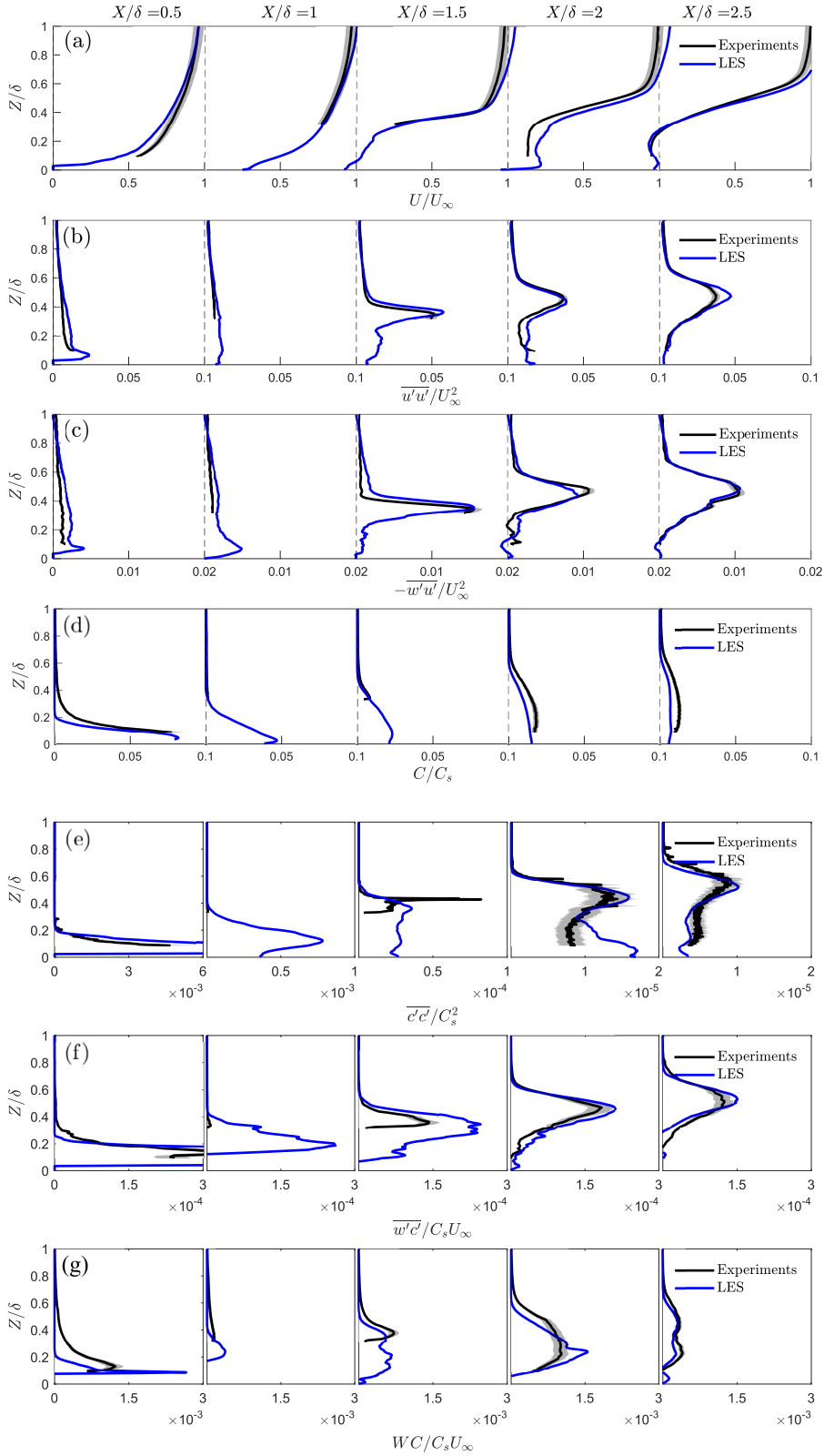


Fig. 8 Water-flume and LES vertical profiles for the LT2400 case (Fig. 2a,d) normalized by their respective length and velocity scales (Section 2.2, 2.3), showing (a) mean velocity, (b) velocity variance, (c) Reynolds shear stress, (d) mean concentration, (e) concentration variance, (f) turbulent scalar flux and (g) advective scalar flux extracted at regular streamwise intervals. Uncertainties (shading) are based on the sum of random and bias errors at 95% confidence interval.

442 The main features of the observed concentration distribution within the rooftop
443 shear layer are qualitatively quite well replicated in the LES, whereas the predicted
444 concentration magnitudes do not agree as well as the velocity statistics. This is at-
445 tributed to the challenges of measuring mean concentrations close to the source in the
446 flume, a thicker averaging plane because of the laser sheet thickness and the difficulty
447 in appropriately scaling the LES concentration statistics. For both the flume and LES,
448 the vertical extent of the mean concentration plume grows strongly after encountering
449 the first tall building. There is a slight difference in the vertical half-width, more
450 noticeable at $X/\delta=3$ (Fig. 7d). The corresponding vertical profiles (Fig. 8d) show the
451 flume measurements always have higher mean concentrations than the LES.

452 Spatial patterns and magnitudes of the concentration variance (Fig. 7e) agree well
453 in most locations that are unaffected by masking, except for the small region within
454 the urban canopy layer at $X/\delta=2$ (Fig. 8e). This region matches poorly because of its
455 proximity to the tall buildings. We note that the concentration variance has a strong
456 dependence on the source properties (Fackrell and Robins, 1982b), and the difference
457 in scale between the flume and LES means this can introduce additional uncertainties.

458 The turbulent scalar fluxes (Fig. 8f) show good agreement except for $X/\delta < 0.5$,
459 where the LES predicts much higher peaks, and at $X/\delta = 1$, where negative fluxes
460 can be observed due to redirected flow by the tall building outside the plane (e.g.
461 Fig. 7a(ii)). The vertical location of the peak in the turbulent scalar flux originating
462 from the tall building is consistent with the peaks in velocity shear, velocity variance,
463 Reynolds stresses, mean concentration and concentration variance, suggesting the
464 first tall building encountered by the incoming flow has the largest overall effect on
465 the incoming flow. The advective scalar flux (Fig. 7g, 8g) is much higher within the
466 canopy layer due to building-induced vertical motions, and this is particularly evident
467 in the LES results (Fig. 7g(ii), 8g) which is not constrained by optical access. From the
468 LES, it is also clear that the advective scalar flux dominates the total scalar transport
469 within the UCL where large magnitudes of vertical and lateral velocities are expected.

470 Given the differences in scale and incoming flow profiles of the flume and LES
471 methods (Section 2; Fig. 4), one may have expected differences in the flow structures.
472 However, only relatively small differences are observed indicating the flow dynamics
473 induced by the roughness elements of the urban model overwhelms any differences
474 between the inflow conditions and that the flow is Reynolds number independent.

475 3.2.1 Rooftop shear layer

476 The rooftop shear layer is responsible for enhanced momentum and scalar transport
477 in all the model geometries. In studies of regular arrays of roughness elements (e.g.
478 Tomas et al., 2017), ‘rooftop shear layer’ is referred to as an ‘internal boundary
479 layer’, but our study has sparse and non-uniform buildings, hence we do not use that
480 terminology.

481 For the detailed LT2400 case (Fig. 7, 8), when the incoming flow impacts the first
482 tall building within the laser sheet plane at $X/\delta = 1.25$, the flow diverges around the
483 side and top of the building. The LES results clearly show an initial separation at the
484 leading edge, reattachment near the trailing edge of the rooftop, and backward flow
485 on the leeward side of the building (Fig. 7a(ii)). These features are obscured in the

486 flume results (Fig. 7a(i)). The literature suggest no reattachment on the sides and roof
487 of isolated buildings with height larger than its streamwise length (Oke et al., 2017).
488 However, the urban model in the current study is much more complex, with upstream
489 neighbourhood buildings (e.g. at $X/\delta=1$) introducing advective fluxes, flow vortices
490 and turbulence to the flow which can encourage reattachment. The velocity profiles
491 (Fig. 8a) have strong shear and inflection points starting from $X/\delta \geq 1.5$. These suggest
492 the presence of Kelvin–Helmholtz instabilities, which is supported by peaks in the
493 vertical profiles of the velocity variance and Reynolds shear stress (Fig. 8b,c) that grow
494 in width with downstream distance. The increased turbulence in the rooftop shear layer
495 is expected to improve vertical scalar bulk transport and contribute significantly to
496 the turbulent fluxes in the roughness sublayer. This is supported by higher turbulent
497 scalar fluxes occurring in the same region for all cases (Fig. 7f, 5f).

498 The magnitudes of the Reynolds shear stress in the rooftop shear layer agree
499 remarkably well with Hertwig et al. (2019) wind-tunnel results from low and (isolated)
500 tall buildings, despite differences in the urban geometry, model scale and experimental
501 method. One notable difference is the vertical location of the peak, whilst Hertwig
502 et al. (2019) finds the rooftop shear layer develops just below the tall building height
503 here the rooftop shear layer develops at and above the building height. This may be
504 because of the differences in both urban morphology (i.e., isolated vs cluster of tall-
505 buildings), experiment inflow and boundary conditions (e.g. $H_{max}/\delta \sim 1$ in Hertwig
506 et al. (2019)), and sparser measurement points from the Laser Doppler Anemometry
507 in Hertwig et al. (2019) compared to PIV. The similarities in Reynolds shear stress
508 magnitude suggest the development of the rooftop shear layer due to the tall building
509 is not very sensitive to the incoming flow conditions. The absence of a secondary
510 peak in the Reynolds shear stress near the ground (as observed by Hertwig et al.
511 (2019)) can be attributed to the porosity of the cluster which reduces the strength of
512 the recirculating flow in its wake.

513 3.2.2 Development of the concentration plume

514 The 3D development of the concentration plume can be examined by extracting the
515 isosurfaces of concentration from the LES results for selected isovalue thresholds
516 (Fig. 9). The low-rise canopy upwind of the tall buildings introduces a strong lateral
517 spread of the plume along the street canyons oriented in the Y direction (Fig. 9).
518 Pollutants can re-circulate in these lateral-canyons and are detrained vertically out of
519 the lower canopy layer before impacting the tall-building cluster further downwind
520 (Fig. 9b). As the plume hits the tall building cluster, there is a rapid increase in the
521 vertical spread of the plume, and the wakes of the tall buildings located furthest
522 upwind interact with downstream low- and high-rise buildings to further alter the
523 cluster near-wake dynamics and plume geometry. The vertical and lateral spread of
524 the plume in the RSL can be attributed to strong updrafts, downdrafts and side-drafts
525 around the tall buildings (expanding the depth of the UCL), as well as flow channelling
526 within the street canyons in the urban canopy. The changes in the mean flow direction
527 and magnitude within the RSL contribute to the advective scalar flux (Fig. 7g). The
528 total scalar transport is also affected by turbulence generated by the low- and high-
529 rise buildings which contributes to the turbulent scalar flux component (Fig. 7f).

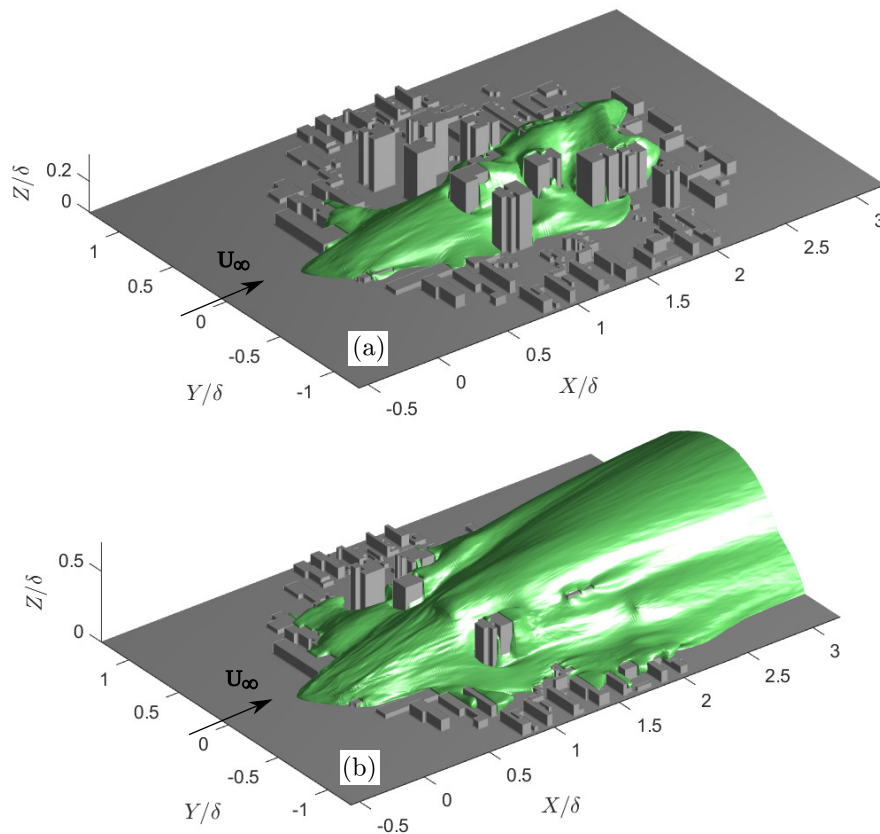


Fig. 9 Isosurfaces of the concentration plume (green) extracted from the LES using isovalues of (a) $C/C_s = 10^{-2}$ and (b) $C/C_s = 10^{-3}$.

530 For accurate prediction of peak concentration levels, it is necessary to consider both
 531 advective and turbulent scalar flux components.

532 3.3 Effects of low-rise neighbouring buildings

533 The influence of the low buildings on the flow is analysed by comparing the simplified
 534 tall-buildings-only (T2400) and more realistic with low-rise building (LT2400) cases.
 535 The mean velocity profiles generally agree well with each other, with the LT2400 case
 536 having slightly higher streamwise velocities at all locations compared to the T2400
 537 case (Fig. 10a). This is attributed to the presence of the low-level canopy in LT2400
 538 which displaces fluid vertically and to the sides due to blockage effects. The velocity
 539 variance and Reynolds shear stress show similar trends, but the peak rooftop shear
 540 layer from the tall buildings is just slightly higher and larger in magnitude for the
 541 T2400 case (Fig. 10b,c). The low-rise canopy in LT2400 has the effect of increasing

the zero-plane displacement, hence the incoming flow experiences a relatively shorter tall-building for LT2400 *cf.* T2400, thus inducing a lower shear layer.

The mean concentration profile trends (Fig. 10d) agree well in most streamwise locations except near $X/\delta = 1.5$ and 2 where higher mean concentrations are seen in the T2400 case *cf.* LT2400 (Fig. 10d). This is attributed to higher level of vertical advection of dye in T2400 (Fig. 10g), which is consistent with the higher shear layer and greater magnitudes of velocity variance and Reynolds shear stress *cf.* LT2400 (Fig. 10c). The presence of low-level canopy in LT2400 also promotes the advection of dye in the lateral direction at the street-level (channelling and branching of the plume along streets and through intersections) which can locally reduce the mean concentration levels. While this is not observed in Fig. 10g due to a lack of optical access, the isosurfaces of the concentration plume from the LES results clearly shows significant advection of dye laterally along the low-rise street canyons (Fig. 9). The concentration variances have large quantitative differences between the two cases. T2400 has similar trends but systematically much larger magnitudes at $X/\delta \geq 1$ *cf.* LT2400. The turbulent scalar fluxes have similar characteristics to the Reynolds stresses, with the T2400 peaks elevated at all distances from the source. The T2400 peak magnitude is also higher due to larger concentration fluctuations (larger concentration variances).

The observation of significant flow advection in the lateral direction (Fig. 9) shows the oncoming flow (and concentration plume) can be significantly altered by the low-rise buildings before it encounters the tall building. Even though the results show tall buildings dominate to a large degree the flow structure in the wake, the effect of the low-rise buildings on the velocity and concentration statistics is non-negligible considering they occupy only a comparatively small portion of the patch (Fig. 2a). Differences in the T2400 and LT2400 velocity and concentration statistics are quantitatively comparable to the differences in the T2400 and T4800 cases (Fig. 6). This suggests the extent of the influence of the low-rise buildings is similar to the impact of the choice of scale on the overall flow field, and clearly not as important as the momentum and scalar fluxes associated with the rooftop shear layer.

4 Conclusions

Pollutant dispersion around a realistic tall-buildings-only cluster (based on a Beijing neighbourhood) is investigated at two scales (T2400 and T4800) using PIV- and PLIF-based flume measurements. This is complemented with an additional case consisting of low-rise buildings surrounded by the tall-building cluster (LT2400), investigated using flume and LES analyses.

Flume observations at two scales (T2400, T4800) find the rooftop shear layer dominates the vertical momentum and scalar fluxes. The magnitude and vertical location of the corresponding peak agree well, with minor differences attributed to differences in the incoming boundary layer thickness (relative to the building height) due to the choice of model scale. Concentration levels decrease with downstream distance due to advective and turbulent scalar transport and at $X/H_{max} = 8$ it has reduced to 1.7% of the source concentration for T4800 and 0.9% for T2400. The concentration variance is found to be highly sensitive to the scale choice due to

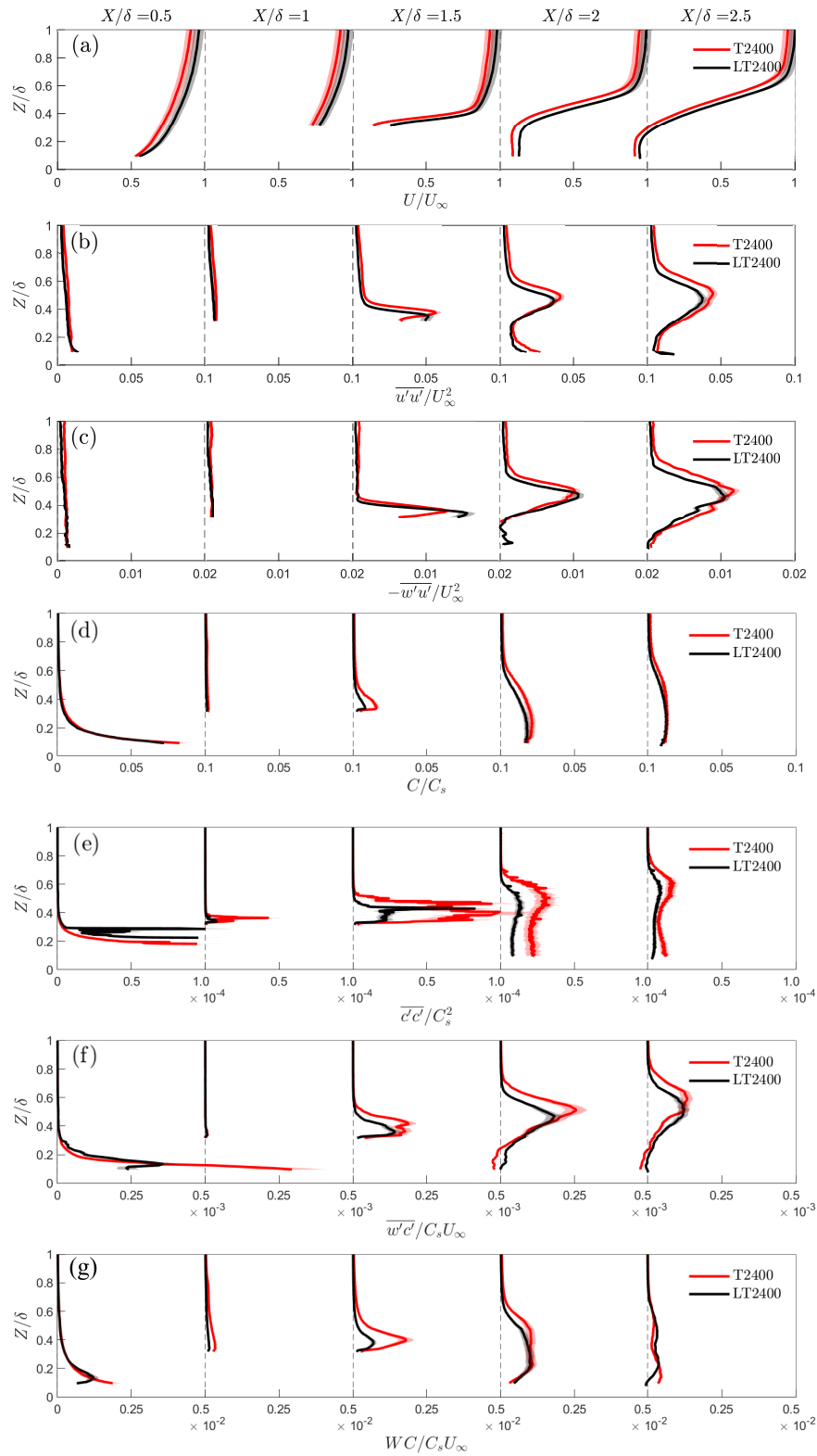


Fig. 10 Water-flume vertical profiles for the T2400 and LT2400 cases, showing normalized (a) mean velocity, (b) velocity variance, (c) Reynolds shear stress, (d) mean concentration, (e) concentration variance, (f) turbulent scalar flux and (g) advective scalar flux extracted at regular streamwise intervals. Uncertainties (shading) are based on the sum of random and bias errors at 95% confidence interval (Appendices B, C).

585 changes in the width of the incoming dye plume. Scale also influences the laser
586 sheet thickness (i.e., relative to building scale), which impacts the processes that are
587 sampled in a very heterogeneous urban settings (as this study). This increases the
588 spatial variability due to significant spatial averaging effects. The influence of scale
589 on the cluster near-wake flow highlight critical details for future flume studies:

- 590 1. Care should be taken to scale the source size and location with respect to the
591 height of the building inducing the rooftop shear layer.
- 592 2. Laser sheet thickness should ideally be an order of magnitude less than the char-
593 acteristic length scale of the model to reduce effects of the spatial-averaging of
594 three-dimensional flow fields.
- 595 3. The scale of the building heights relative to the depth of the log-law region of the
596 incoming boundary layer and the inclusion of low buildings in the urban model
597 are important to capture the peaks in momentum and scalar fluxes accurately.

598 The velocity and concentration statistics for the LT2400 case have good agreement
599 between flume and LES results in most parts of the analysis domain. Notably, the
600 development of the rooftop shear layer and its associated vertical momentum and
601 scalar fluxes have remarkable agreement in both magnitude and position of the peak
602 despite differences in the scale and incoming flow conditions. The concentration levels
603 decrease to approximately 1.1% of the source concentration in the experiment and
604 0.5% for LES at $X/H_{max} = 8$. Minor differences in the concentration statistics are
605 attributed to the variability introduced by differences in the scale and inflow profile.
606 The magnitude of the vertical momentum flux also agrees well with the [Hertwig
607 et al. \(2019\)](#) results for a low and (isolated) tall building. Only the vertical location
608 of the peak differed slightly between the two studies despite differences in urban
609 morphology, model scale and experimental method. It is concluded that the inflow
610 conditions do not appear to be crucial in the development of the rooftop shear layer.

611 Flume observations of LT2400 and T2400 reveal non-negligible effects of the
612 low-rise buildings on the velocity and concentration statistics, with LT2400 having
613 higher streamwise velocities above the UCL due to fluid displacement by the low-
614 level canopy, and lower concentration levels in the measurement plane due to increased
615 advection of the plume in the lateral direction at the street-level. These differences
616 are quantitatively comparable to those observed between T2400 and T4800, and it is
617 concluded that the extent of the influence of the low-rise buildings is similar to the
618 impact of the choice of scale on the overall flow field.

619 There are a number of key findings with general applicability to studies of dis-
620 persion in real urban areas. Firstly, tall buildings expand the depth of the UCL and
621 introduce strong flow disturbances in the RSL, which dominate over differences in
622 initial flow conditions and influences of the low-rise buildings. We conclude that
623 for urban canopy model parametrisations (as needed for weather and climate mod-
624 elling), inclusion of the impact of building-height heterogeneity is clearly important.
625 Secondly, below the mean canopy height, advective fluxes in the lateral direction are
626 significant, which can be difficult to model as they are geometry dependent. Thirdly, in
627 regions with strong flow shear, the turbulent scalar transport is larger than the advective
628 scalar transport. These findings show complex (but realistic) urban areas introduce
629 additional challenges that need to be addressed in model prediction. This will be es-

pecially important if models that lack building-induced flow effects parametrisations are used to simulate dispersion.

Further studies on the impact of building-height heterogeneity that allow for systematic testing are clearly required to develop and/or enhance model parametrisations of roughness sublayer or urban canopy layer flow fields. Specific test cases based on realistic geometries, as presented in this study, are essential to evaluate such parametrisations. The data derived here, and the clear need for future studies of this type, are critical to making weather and climate model predictions more realistic over urban areas, with implications for other aspects of urban modelling (e.g. dispersion or air quality simulations). Further studies in the Beijing tall-building cluster will address the impact of wind direction and the implications for the interaction between the wakes of tall buildings of different heights.

Acknowledgements We would like to acknowledge the contributions from Matthew Coburn and George Meachim who helped collect the data from the flume measurements at the University of Southampton, as well as Yue Yang and Xiaoxue Wang who conducted preliminary analyses of these data sets at the University of Reading.

C.V. gratefully acknowledges the support from her UKRI Future Leader's Fellowship. S.G., M.R., T.G. and D.H. also gratefully acknowledge support from the UK-China Research & Innovation Partnership Fund through the Met Office Climate Science for Service Partnership (CSSP) China as part of the Newton Fund. C.V., S.G., D.H. and H.G. are also grateful for the UK Fluids Network short research visit fund which supported this cross-university collaboration.

Appendix

A Determination of the friction velocity in the flume

The friction velocity in the water flume, $U_{\tau\text{EXP}}$, is determined using two methods. First, data are fit to the log-law equation for smooth walls: $U^+ = (1/\kappa)\ln(Z^+) + B$ where $U^+ = U/U_{\tau\text{EXP}}$ and $Z^+ = ZU_{\tau\text{EXP}}/\nu$. Using $\kappa = 0.4$ for the von Kármán constant and $B=5$ for the smooth-wall intercept. The calculated friction velocity is $U_{\tau}=0.019 \text{ m s}^{-1}$.

Second, the total stress is calculated at the plateau of the Reynolds shear stress profile in the overlap region of the boundary layer (Figure 4) using: $U_{\tau\text{EXP}} = \sqrt{-u'w'}$ under the constant stress assumption. The friction velocity from this method is $U_{\tau}=0.0156 \text{ m s}^{-1}$.

The average of both is taken as the friction velocity, i.e., $U_{\tau\text{EXP}} = 0.0173 \text{ m s}^{-1} \pm 10\%$. The depth of the log-law region is estimated to be within the range $3 \text{ mm} \leq Z \leq 18 \text{ mm}$ ($0.04 < Z/\delta_{\text{EXP}} < 0.22$).

B PIV processing and uncertainty analysis

All image processing procedures for PIV use LaVision's Davis 8.4.0 software (LaVision GmbH, 2019). To pre-process the particle images, the 'subtract time filter' is set to 5 images and 'subtract sliding background scale' set to 8 pixels. Geometrical masking is performed on the measurement plane to remove buildings that block the camera's view and in regions with unavoidable laser reflections. Multi-grid two-pass cross-correlation analysis is performed on the PIV images using a 50% overlap ratio. The final interrogation window size is 24×24 pixels. This translates to a vector resolution of $R_{PIV}=0.8 \text{ mm}$.

For vector post-processing, Davis 8.4.0's 'allowable vector range' is used to remove spurious vectors if above 12 pixel shifts. Vectors with correlation value below 0.7 are deleted, and the 'universal outlier detection' routine is used to remove vectors if residual is above 2 in a 5×5 filter region. The neighbourhood interpolation scheme is used to fill the missing vectors. Spatial smoothing is performed to generate the final vector fields.

674 The main source of systematic error leading to velocity bias is expected to arise from the image
 675 scaling procedure. It is estimated to be $\sim 1.3\%$. For each case, 2,000 vector fields are used to obtain the
 676 velocity statistics. The standard deviation (turbulence intensity) of the streamwise fluctuating velocity in
 677 the freestream is 1.2%. For the 1:2400 (or 1:4800) scale models, the total measurement time at full-scale
 678 is 21.7 h (or 43.4 h) and the temporal spacing between consecutive vector fields is 39 s (or 78 s).

679 C PLIF processing and uncertainty analysis

680 For PLIF, the fluorescence intensity measured at every pixel of the camera is expected to be a linear function
 681 of the local dye concentration multiplied by the local laser intensity. In this PLIF setup, the local laser
 682 intensity is constant and any pulse-to-pulse variations in the laser power are accounted for by monitoring the
 683 energy of each laser pulse with an energy monitor (E_{ref}). The calibration procedure obtains the coefficients
 684 of the linear mapping function from fluorescence intensity to local concentration for each camera pixel.

685 A background measurement is obtained with $C_0=0$ mg L⁻¹. Two small calibration tanks with two
 686 known concentrations of the dye ($C_1=0.03$ mg L⁻¹ and $C_2=0.05$ mg L⁻¹) are sequentially inserted into the
 687 water flume and aligned with the laser sheet. Calibration images of the uniform concentrations (I_0 , I_1 and
 688 I_2) are captured and post-processed to calculate the calibration coefficient, i.e., $A_{cal} = (A_1 + A_2)/2$, where
 689 $A_{i=1,2} = (C_{i=1,2} - C_0)/(I_{i=1,2}^c/E_{ref} - I_0)$. Here, I_i^c represents the image intensity in the calibration images
 690 corrected for light attenuation along the light path and secondary fluorescence (Vanderwel and Tavoularis,
 691 2014), and E_{ref} accounts for pulse-to-pulse variations in the laser power captured by the energy monitor of
 692 the laser. The final concentration field is obtained by applying the calibration coefficient to the raw PLIF
 693 image, I , via $C = (I/E_{ref} - I_0)A_{cal}$.

694 Using three known calibration concentrations (i.e., C_0, C_1, C_2) to determine the linear calibration
 695 coefficient permits an estimate of the uncertainty associated with this fit. The error associated with the
 696 mapping coefficients is estimated by defining the error term as: $\epsilon = (\epsilon_1 + \epsilon_2)/2$, where $\epsilon_{i=1,2} = (I_{i=1,2}^c -$
 697 $I_0)A_{cal} - C_{i=1,2}$, and computing the mean and standard deviation of the error term for the entire image
 698 excluding the borders. We estimate the potential bias error to be 0.8% and the potential random error as
 699 5.3% (or 10.6% for a 95% confidence interval). The effects of secondary fluorescence may locally increase
 700 measurement uncertainties in some regions (Sections 3.1 and 3.2) but are not explicitly corrected here as
 701 they require non-trivial methods to account for non-linear effects. The spatial resolution of the PLIF results
 702 is $R_{PLIF}=0.0665$ mm.

703 Geometrical masking is performed on the PLIF results. As the PLIF camera position relative to the
 704 buildings is different from the PIV setup, the buildings masked may appear to be slightly different because
 705 of the change in perspective. The masking procedure is performed on buildings in the laser sheet's plane, at
 706 boundaries where the laser reflection cannot be avoided and on buildings (outside the laser sheet's plane)
 707 that obstructed the camera's line-of-sight.

708 The PIV vector fields and PLIF concentration fields have different coordinate systems and vastly
 709 different spatial resolutions due to the use of interrogation windows in PIV's cross-correlation analysis.
 710 To calculate the joint velocity-concentration statistics, inhouse code maps the PIV and PLIF coordinates
 711 to a common coordinate system via linear interpolation. The mapped concentration field is sub-sampled
 712 to the PIV's resolution after neighbourhood averaging using a box kernel with dimensions equivalent
 713 to R_{PIV}/R_{PLIF} , and selecting the concentration values at the points of the common coordinate system.
 714 The accuracy of the overlap of the coordinate system mapping is estimated to be within $3R_{PLIF}$. This is
 715 mitigated by the neighbourhood averaging and subsampling procedures and hence negligible. The combined
 716 uncertainty of the joint velocity-concentration statistics is estimated to lead to a systematic error of up to
 717 11.9% in the measured scalar fluxes.

718 References

- 719 Baik JJ, Park RS, Chun HY, Kim JJ (2000) A laboratory model of urban street-canyon flows. *J Appl*
 720 *Meteorol* 39(9):1592–1600
 721 Baj P, Bruce PJK, Buxton ORH (2016) On a plif quantification methodology in a nonlinear dye response
 722 regime. *Exp Fluids* 57(6):106

- 723 Barlow J, Best M, Bohnenstengel SI, Clark P, Grimmond S, Lean H, Christen A, Emeis S, Haeffelin
724 M, Harman IN, Lemonsu A, Martilli A, Pardyjak E, Rotach MW, Ballard S, Boutle I, Brown A, Cai
725 X, Carpentieri M, Coceal O, Crawford B, Sabatino SD, Dou J, Drew DR, Edwards JM, Fallmann J,
726 Fortuniak K, Gornall J, Gronemeier T, Halios CH, Hertwig D, Hirano K, Holtslag AAM, Luo Z, Mills
727 G, Nakayoshi M, Pain K, Schlünzen KH, Smith S, Soulhac L, Steeneveld GJ, Sun T, Theeuwes NE,
728 Thomson D, Voogt JA, Ward HC, Xie ZT, Zhong J (2017) Developing a research strategy to better
729 understand, observe, and simulate urban atmospheric processes at kilometer to subkilometer scales.
730 *Bull Am Meteor Soc* 98(10)
- 731 Belcher SE (2005) Mixing and transport in urban areas. *Philos T Roy Soc A* 363(1837):2947–2968
- 732 Britter RE, Hanna SR (2003) Flow and dispersion in urban areas. *Annu Rev Fluid Mech* 35:469–496
- 733 Brixey LA, Heist DK, Richmond-Bryant J, Bowker GE, Perry SG, Wiener RW (2009) The effect of a
734 tall tower on flow and dispersion through a model urban neighborhood Part 2. Pollutant dispersion. *J*
735 *Environ Monit* 11:2171–2179
- 736 Castro IP, Robins AG (1977) The flow around a surface-mounted cube in uniform and turbulent streams.
737 *Journal of Fluid Mechanics* 79(2):307–335, DOI 10.1017/S0022112077000172
- 738 Di Bernardino A, Monti P, Leuzzi G, Querzoli G (2015) Water-channel study of flow and turbulence past
739 a two-dimensional array of obstacles. *Boundary-Layer Meteorol* 155:73–85
- 740 Elshaer A, Gairola A, Adamek K, Bitsuamlak G (2017) Variations in wind load on tall buildings due to
741 urban development. *Sustainable Cities and Society* 34:264–277
- 742 Fackrell J, Robins A (1982a) Concentration fluctuations and fluxes in plumes from point sources in a
743 turbulent boundary layer. *J Fluid Mech* 117:1–26
- 744 Fackrell J, Robins A (1982b) The effects of source size on concentration fluctuations in plumes. *Boundary-*
745 *Layer Meteorol* 22(3):335–350
- 746 Fuka V, Xie ZT, Castro IP, Hayden P, Carpentieri M, Robins AG (2018) Scalar fluxes near a tall building
747 in an aligned array of rectangular buildings. *Boundary-Layer Meteorol* 167:53–76
- 748 Giometto M, Christen A, Meneveau C, Fang J, Krafczyk M, Parlange MB (2016) Spatial characteristics of
749 roughness sublayer mean flow and turbulence over a realistic urban surface. *Boundary-Layer Meteorol*
750 160:425–452
- 751 Grimmond C, Best M, Barlow J, Arnfield AJ, Baik JJ, Baklanov A, Belcher S, Bruse M, Calmet I, Chen F,
752 Clark P, Dandou A, Erell E, Fortuniak K, Hamdi R, Kanda M, Kawai T, Kondo H, Krayenhoff S, Lee
753 SH, Limor SB, Martilli A, Masson V, Miao S, Mills G, Moriwaki R, Oleson K, Porson A, Sievers U,
754 Tombrou M, Voogt J, Williamson T (2009) Urban surface energy balance models: Model characteristics
755 and methodology for a comparison study. In: Baklanov A, Sue G, Alexander M, Athanassiadou M
756 (eds) *Meteorological and Air Quality Models for Urban Areas*, Springer Berlin Heidelberg, Berlin,
757 Heidelberg, pp 97–123, DOI 10.1007/978-3-642-00298-4_11
- 758 Grimmond S, Bouchet V, Molina LT, Baklanov A, Tan J, Schlünzen KH, Mills G, Golding B, Masson V,
759 Ren C, Voogt J, Miao S, Lean H, Heusinkveld B, Hovespyan A, Teruggi G, Parrish P, Joe P (2020)
760 Integrated urban hydrometeorological, climate and environmental services: Concept, methodology and
761 key messages. *Urban Climate* 33:100,623, DOI <https://doi.org/10.1016/j.uclim.2020.100623>
- 762 Grylls T (2020) Simulating air pollution in the urban microclimate. PhD thesis, Imperial College London
- 763 Grylls T, Le Cornec CM, Salizzoni P, Soulhac L, Stettler MEJ, van Reeuwijk M (2019) Evaluation of an
764 operational air quality model using large-eddy simulation. *Atmospheric Environment: X* 3:100,041
- 765 Heist DK, Brixey LA, Richmond-Bryant J, Bowker GE, Perry SG, Wiener RW (2009) The effect of a
766 tall tower on flow and dispersion through a model urban neighborhood Part 1. Flow characteristics. *J*
767 *Environ Monit* 11:2163–2170
- 768 Hertwig D, Gough HL, Grimmond S, Barlow JF, Kent CW, Lin WE, Robins AG, Hayden P (2019) Wake
769 characteristics of tall buildings in a realistic urban canopy. *Boundary-Layer Meteorol* 172(2):239–270
- 770 Hertwig D, Gough HL, Grimmond S, Vanderwel C (2020) Dataset: Water-flume model geometries of a
771 tall- building cluster in Beijing. DOI 10.5281/zenodo.3768763
- 772 Hertwig D, Grimmond S, Kotthaus S, Vanderwel C, Gough H, Haeffelin M, Robins A (2021) Variability of
773 physical meteorology in urban areas at different scales: implications for air quality. *Faraday Discussions*
774 226:149–172
- 775 Heus T, Vilà-Guerau de Arellano J, De Roode S, Pino González D, Van Heerwaarden CC, Jonker HJJ,
776 Siebesma P, Axelsen S, Van den Dries K, Geoffroy O, et al. (2010) Formulation of the dutch atmo-
777 spheric large-eddy simulation (dales) and overview of its applications. *Geoscientific Model Development*
778 3(2):415–444
- 779 Hunt JCR, Abell CJ, Peterka JA, Woo H (1978) Kinematical studies of the flows around free or surface-
780 mounted obstacles; applying topology to flow visualization. *Journal of Fluid Mechanics* 86:179–200,

- DOI 10.1017/S0022112078001068
- 781 Kanda M (2006) Progress in the scale modeling of urban climate: Review. *Theoretical and Applied*
782 *Climatology* 84:23–33, DOI <https://doi.org/10.1007/s00704-005-0141-4>
- 783 Kanda M, Inagaki A, Miyamoto T, Gryschka M, Raasch S (2013) A new aerodynamic parametrization for
784 real urban surfaces. *Boundary-Layer Meteorol* 148(2):357–377
- 785 Kent CW, Grimmond S, Barlow J, Gatey D, Kotthaus S, Lindberg F, Halios CH (2017) Evaluation of urban
786 local-scale aerodynamic parameters: Implications for the vertical profile of wind speed and for source
787 areas. *Boundary-Layer Meteorology* 164:183–213, DOI <https://doi.org/10.1007/s10546-017-0248-z>
- 788 Kent CW, Grimmond S, Gatey D, Hirano K (2019) Urban morphology parameters from global digital
789 elevation models: Implications for aerodynamic roughness and for wind-speed estimation. *Remote*
790 *Sensing of Environment* 221:316–339, DOI <https://doi.org/10.1016/j.rse.2018.09.024>
- 791 LaVision GmbH G (2019) Product-Manual for DaVis 8.4
- 792 Lean HW, Barlow JF, Halios CH (2019) The impact of spin-up and resolution on the representation of
793 a clear convective boundary layer over London in order 100-m grid-length versions of the Met Office
794 Unified Model. *Q J Roy Meteor Soc* 145(721):1674–1689
- 795 Letzel MO, Krane M, Raasch S (2008) High resolution urban large-eddy simulation studies from street
796 canyon to neighbourhood scale. *Atmospheric Environment* 42(38):8770–8784
- 797 Macdonald R, Griffiths R, Hall D (1998) An improved method for the estimation of surface roughness of
798 obstacle arrays. *Atmospheric Environment* 32(11):1857–1864
- 799 Marucci D, Carpentieri M (2020) Dispersion in an array of buildings in stable and convective atmo-
800 spheric conditions. *Atmospheric Environment* 222:117,100, DOI <https://doi.org/10.1016/j.atmosenv.2019.117100>
- 801 Masson V (2006) Urban surface modeling and the meso-scale impact of cities. *Theor Appl Climatol*
802 84:35–45
- 803 Nazarian N, Martilli A, Kleissl J (2018) Impacts of realistic urban heating, part i: spatial variability of
804 mean flow, turbulent exchange and pollutant dispersion. *Boundary-Layer Meteorol* 166(3):367–393
- 805 Nicolai C, Taddei S, Manes C, Ganapathisubramani B (2020) Wakes of wall-bounded turbulent flows past
806 patches of circular cylinders. *J Fluid Mech* 892
- 807 Nozu T, Tamura T, Takeshi K, Akira K (2015) Mesh-adaptive les for wind load estimation of a high-rise
808 building in a city. *J Wind Eng Ind Aerodyn* 144:62–69
- 809 Oke TR, Mills G, Christen A, Voogt JA (2017) *Airflow*. Cambridge University Press, p 77–121. DOI
810 [10.1017/9781139016476.005](https://doi.org/10.1017/9781139016476.005)
- 811 Plate EJ (1999) Methods of investigating urban wind fields—physical models. *Atmospheric Environment*
812 33(24–25):3981–3989
- 813 Pournazeri S, Princevac M, Venkatram A (2012) Scaling of building affected plume rise and dispersion in
814 water channels and wind tunnels—revisit of an old problem. *J Wind Eng Ind Aerodyn* 103:16–30
- 815 Saathof P, Stathopoulos T, Dobrescu M (1995) Effects of model scale in estimating pollutant dispersion
816 near buildings. *J Wind Eng Ind Aerodyn* 54–55:549–559
- 817 Sessa V, Xie ZT, Herring S (2018) Turbulence and dispersion below and above the interface of the internal
818 and the external boundary layers. *Journal of Wind Engineering and Industrial Aerodynamics* 182:189–
819 201
- 820 Simpson RL (2001) Junction flows. *Annu Rev Fluid Mech* 33(1):415–443
- 821 Suter I (2018) *Simulating the impact of blue-green infrastructure on the microclimate of urban areas*. PhD
822 thesis, Imperial College London
- 823 Sützl B, Rooney G, van Reeuwijk M (2021) Drag distribution in idealized heterogeneous urban environ-
824 ments. *Boundary-Layer Meteorol* 178:225–248
- 825 Tanaka S, Murata S (1999) An investigation of the wake structure and aerodynamic characteristics of a
826 finite circular cylinder: time-averaged wake structures behind circular cylinders with various aspect
827 ratios. *JSME International Journal Series B Fluids and Thermal Engineering* 42(2):178–187
- 828 Toliás I, Koutsourakis N, Hertwig D, Efthimiou G, Venetsanos A, Bartzis J (2018) Large eddy simulation
829 study on the structure of turbulent flow in a complex city. *J Wind Eng Ind Aerodyn* 177:101–116
- 830 Tomas JM, Pourquie MJB, Jonker HJJ (2015) The influence of an obstacle on flow and pollutant dispersion
831 in neutral and stable boundary layers. *Atmospheric Environment* 113:236–246
- 832 Tomas JM, Eisma HE, Pourquie MJB, Elsinga GE, Jonker HJJ, Westerweel J (2017) Pollutant dispersion
833 in boundary layers exposed to rural-to-urban transitions: Varying the spanwise length scale of the
834 roughness. *Boundary-Layer Meteorol* 163(2):225–251
- 835 Torres P, Le Clainche S, Vinuesa R (2021) On the experimental, numerical and data-driven methods to
836 study urban flows. *Energies* 14(5):1310

- 839 Uno I, Wakamatsu S, Ueda H, Nakamura A (1988) An observational study of the structure of the nocturnal
840 urban boundary layer. *Boundary-Layer Meteorol* 45(1-2):59–82
- 841 Vanderwel C, Ganapathisubramani B (2019) Turbulent boundary layers over multiscale rough patches.
842 *Boundary-Layer Meteorology* 172(1):1–16
- 843 Vanderwel C, Tavoularis S (2014) Measurements of turbulent diffusion in uniformly sheared flow. *J Fluid*
844 *Mech* 754:488–514
- 845 Vanderwel C, Tavoularis S (2016) The fine structure of a slender scalar plume in sheared turbulence. In:
846 *Progress in Turbulence VI*, Springer, pp 259–263
- 847 Vreman AW (2004) An eddy-viscosity subgrid-scale model for turbulent shear flow: Algebraic theory and
848 applications. *Phys Fluids* 16(10):3670–3681
- 849 Wang H, Zhou Y (2009) The finite-length square cylinder near wake. *J Fluid Mech* 638:453
- 850 Wang H, Zhou Y, Chan C, Lam KS (2006) Effect of initial conditions on interaction between a boundary
851 layer and a wall-mounted finite-length-cylinder wake. *Phys Fluids* 18(6):065,106
- 852 Wang ZY, Plate EJ, Rau M, Keiser R (1996) Scale effects in wind tunnel modelling. *J Wind Eng Ind*
853 *Aerodyn* 61(2):113–130
- 854 Yan B, Li Q (2016) Large-eddy simulation of wind effects on a super-tall building in urban environment
855 conditions. *Structure and Infrastructure Engineering* 12(6):765–785